European Journal of Mechanics A/Solids 62 (2017) 1–13

Contents lists available at ScienceDirect

European Journal of Mechanics A/Solids

journal homepage: www.elsevier.com/locate/ejmsol

A plane strain elasticity model for the acoustical properties of rib-stiffened composite plates

Fengxian Xin [a, b, *], Tian Jian Lu [a, b, **]

[a] State Key Laboratory for Strength and Vibration of Mechanical Structures, Xi'an Jiaotong University, Xi'an, 710049, PR China
[b] MOE Key Laboratory for Multifunctional Materials and Structures, Xi'an Jiaotong University, Xi'an, 710049, PR China

ARTICLE INFO

Article history:
Received 26 July 2016
Received in revised form
1 November 2016
Accepted 4 November 2016
Available online 9 November 2016

Keywords:
Plates
Vibration
Analytical modeling

ABSTRACT

A theoretical elasticity model is established to study the noise reduction performance of a compliant coating layer that is attached to a periodically rib-stiffened plate under time-harmonic mechanical excitation. The general case of the structure immersed in two different fluids is considered so as to accurately simulate the interior and exterior fluid media of hull structures in underwater environment. The theory of plane strain elasticity is employed to model the dilatational and shear motions of the compliant coating layer and the elastic plate, while the scalar Helmholtz equation is adopted to describe the motions of the two fluids. Vibroacoustic coupling is realized by enforcing displacement and stress continuity at adjacent layer interfaces, with the reaction forces of the rib-stiffeners accounted for by introducing them as discretely distributed stresses. The resultant boundary value equations of the system are solved by applying the Fourier transform technique, based upon which the noise reduction due to the compliant coating layer can be favorably calculated. Numerical investigations are implemented to explore the effects of coating thickness, coating material properties, radiation angle, and excitation location on noise reduction. The theoretical results presented in this study provide valuable guidance for experimental research and structural design related to the decoupling effects of coating layers affixed to elastic structures in underwater environment.

1. Introduction

The combined mechanical and acoustic performance of composite structures is of great concern in many engineering applications, since these structures are often subjected to dynamic and acoustic excitations (Ehsan Omidi, 2016; Li et al., 2013; Li and Lyu, 2014; Reza Ansari, 2016; Xin and Lu, 2016; Chen and Huang, 2015). Among these, noise reduction by compliant coating layers attached to underwater structures for enhanced structure sound proofing has received increasing attention (Hladky-Hennion and Decarpigny, 1991; Keltie, 1998; Tao et al., 2010). The coating layer made of a relatively soft material contributes to enlarge the thickness deformation over the elastic structure under fluid loading, causing therefore the decoupling of the motions of the elastic structure and the surrounding fluid (Berry et al., 2001; Foin et al., 2000). The acoustic design of such coated structures calls for accurate theoretical modeling of the noise reduction response of the compliant coating layer. The purpose of this paper is therefore to develop a theoretical elasticity model for noise reduction achieved by attaching a compliant coating layer to a periodically rib-stiffened plate immersed in fluids.

A great deal of work has been devoted to studying the mechanical and acoustical performance of composite structures. For instance, a layerwise/solid-element approach was proposed to analyze the linear static and free vibration of composite sandwich plates (Hasheminejad and Miri, 2007; Li et al., 2013; Pandey and Pradyumna, 2015; Sadeghpour et al., 2016; Sahoo et al., 2016). The soundproofing effect of particle composites was experimentally studied, and concluded that the transmission loss of the composites was increased nonlinearly with increasing filler volume fraction (Liang and Jiang, 2012). Also, the mechanical, thermal and acoustical performances of composites were experimentally investigated from the viewpoint of manufacturing conditions

* Corresponding author. State Key Laboratory for Strength and Vibration of Mechanical Structures, Xi'an Jiaotong University, Xi'an, 710049, PR China.
** Corresponding author. State Key Laboratory for Strength and Vibration of Mechanical Structures, Xi'an Jiaotong University, Xi'an, 710049, PR China
E-mail addresses: fengxian.xin@gmail.com (F. Xin), tjlu@mail.xjtu.edu.cn (T.J. Lu).

http://dx.doi.org/10.1016/j.euromechsol.2016.11.001
0997-7538/

(David and Francesco, 2015; Hao et al., 2013).

Actually, the Kirchhoff thin plate theory was commonly adopted to model the vibration and acoustic responses of single- or multi-layer panel configurations (Keltie, 1993; Legault and Atalla, 2010; Lin and Garrelick, 1977; Mace, 1980; Narayanan and Shanbhag, 1981; Xin and Lu, 2010a). To account for the influence of shearing deformation and rotary inertia, the Mindlin plate theory was developed for modeling thick plates (Gholami et al., 2016; Mindlin, 1951; Park and Mongeau, 2008). To more accurately describe three-dimensional (3D) displacements and stresses, the elasticity theory of solids should be employed to handle the dilatational and shear wave behaviors of solid layers (Ko, 1997; Maidanik and Tucker, 1974; Qu and Meng, 2014). This is of vital importance for obtaining exact predictions at higher wavenumbers and frequencies, as plate theories failed to do so.

Adopting the elasticity theory, Jackins and Gaunaurd formulated a theoretical model for sound reflection from multilayered elastic flat plates (Jackins and Gaunaurd, 1986), while Chonan and Kugo conducted an acoustic design for three-layered plates with high sound interception in terms of various combinations of the facing and the core materials (Chonan and Kugo, 1991). Ko established a theoretical model to evaluate the effectiveness of an air-voided elastomer layer perfectly bonded to an infinite plate in reducing the structure-borne noise (Ko, 1997). Often, to deal with plate structures covered with coating layers, the elasticity theory was also combined with the thin plate theory, yielding sufficiently accurate results. For instance, focusing on the signal velocity response of elastically coated plates, Keltie developed an analytical model for a compliant elastic coating attached to a submerged thin plate (Keltie, 1998). Modeling the decoupling layer with 3D elasticity theory, Berry et al. presented a theoretical analysis for the vibroacoustic response of a finite simply-supported rectangular plate covered by a decoupling layer and immersed in heavy fluid.

Although the sound radiation and transmission issues of elastically coated plate structures have been extensively studied, the noise reduction realized by attaching a compliant coating layer to a plate structure (periodically rib-stiffened plate in particular) is rarely studied. Since the relationship between noise reduction and sound transmission loss has not been clearly explained (Tao et al., 2010), an individual investigation for the noise reduction behavior of the compliant coating layer is of paramount importance to understand the soundproofing effectiveness of the coating. This study aims to squarely address this issue. By utilizing the Fourier transform technique, a 3D elasticity model is proposed to explore the noise reduction of a compliant coating layer affixed to a rib-stiffened plate. The model is capable of dealing with the case that the structure is immersed in two different fluids on its two sides, which thus can favorably simulate the real environment of underwater structures. For illustration, numerical investigations are conducted to quantify the effects of key system parameters (e.g., coating thickness, radiation angle, coating material properties and excitation location) on the noise reduction of the compliant coating layer.

2. Theoretical formulation

2.1. Structure dynamics of plate and coating

With reference to Fig. 1, consider a periodically rib-stiffened elastic plate of infinite extent in the *xz* plane covered with a uniform coating layer of a compliant, elastic solid on the upper surface. These rib-stiffeners are parallelly connected with the elastic plate along the *z*-direction, separated by a constant distance of *L* in the *x*-direction. The entire structure is immersed in two different fluids, i.e., fluid 1 on the lower half-space and fluid 2 on the upper half-space. The thicknesses of the compliant coating layer and the elastic plate are represent by the symbols h_t and h_b, while the height and thickness of the rib-stiffeners are denoted by h_r and t, respectively. A line time-harmonic force $f(x,t)$ along the *z*-direction is assumed to exert on the bottom of the elastic plate, causing the vibration of the structure and sound radiation in both the lower and upper half-spaces.

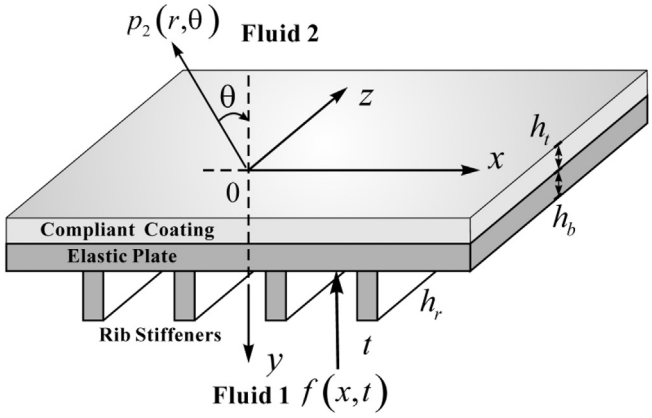

Fig. 1. Schematic illustration for noise reduction of a rib-stiffened plate covered with a compliant coating layer.

Both made of linear, isotropic and homogeneous solid materials, the motions of the compliant coating layer and the elastic plate should obey the Navier-Cauchy equation in the category of elasticity theory, as:

$$\mu_a \nabla^2 \mathbf{u}^{(a)} + (\lambda_a + \mu_a)\nabla\left(\nabla \cdot \mathbf{u}^{(a)}\right) = \rho_a \frac{\partial^2 \mathbf{u}^{(a)}}{\partial t^2} \tag{1}$$

where $\mathbf{u}(x,y,t)$ is the displacement vector, λ_a and μ_a are the Lamé constants, ρ_a denotes alternatively the density for the compliant coating layer and the elastic plate when its subscript $a = t$ and $a = b$. The same meaning of the subscript holds throughout the study. The stresses and strains in the elastic solid layers comply with the following constitutive relationship:

$$\sigma_{ij}^{(a)} = \lambda_a\left(\nabla \cdot \mathbf{u}^{(a)}\right)\delta_{ij} + \mu_a\left(u_{i,j}^{(a)} + u_{j,i}^{(a)}\right) \tag{2}$$

To describe the dilatational motion and shear motion of a solid, the elasticity theory dictates that the displacement of the solid can be divided into the irrotational part and the rotational part (corresponding separately to dilatational motion and shear motion), as:

$$\mathbf{u}^{(a)} = \nabla\phi^{(a)} + \nabla \times \psi^{(a)} \tag{3}$$

where $\phi^{(a)}$ is the dilatational scalar potential and ψ is the shear vector potential. Given the two-dimensional (2D) plane strain nature of the system, the shear vector potential ψ actually has only one component in the *z*-direction, i.e., taking the form of $(0, 0, \psi^{(a)})$. The two potentials are separately governed by the Helmholtz equation:

$$\nabla^2\phi^{(a)} = \frac{1}{\left[c_d^{(a)}\right]^2}\frac{\partial^2\phi^{(a)}}{\partial t^2}, \quad \nabla^2\psi^{(a)} = \frac{1}{\left[c_s^{(a)}\right]^2}\frac{\partial^2\psi^{(a)}}{\partial t^2} \tag{4}$$

in which the dilatational wave speed and the shear wave speed are determined by the Lamé constants and the density of the solid material, as:

$$c_d^{(a)} = \sqrt{\frac{\lambda_a + 2\mu_a}{\rho_a}}, \quad c_s^{(a)} = \sqrt{\frac{\mu_a}{\rho_a}} \tag{5}$$

To relate variables in the physical domain to those in the wavenumber domain, the Fourier transform technique is applied, yielding:

$$\phi^{(a)}(x,y,t) = \frac{1}{2\pi}\int_{-\infty}^{+\infty} \Phi^{(a)}(\alpha,y,t)e^{-i\alpha x}d\alpha, \quad \Phi^{(a)}(\alpha,y,t) = \int_{-\infty}^{+\infty} \phi^{(a)}(x,y,t)e^{i\alpha x}dx \tag{6}$$

$$\psi^{(a)}(x,y,t) = \frac{1}{2\pi}\int_{-\infty}^{+\infty} \Psi^{(a)}(\alpha,y,t)e^{-i\alpha x}d\alpha, \quad \Psi^{(a)}(\alpha,y,t) = \int_{-\infty}^{+\infty} \psi^{(a)}(x,y,t)e^{i\alpha x}dx \tag{7}$$

Accordingly, the Helmholtz equation of Eq. (4) can be written in the wavenumber domain as:

$$\frac{d^2\Phi^{(a)}}{dy^2} + \left(\left[k_d^{(a)}\right]^2 - \alpha^2\right)\Phi^{(a)} = 0 \tag{8}$$

$$\frac{d^2\Psi^{(a)}}{dy^2} + \left(\left[k_s^{(a)}\right]^2 - \alpha^2\right)\Psi^{(a)} = 0 \tag{9}$$

where $k_d^{(a)} = \omega/c_d^{(a)}$ and $k_s^{(a)} = \omega/c_s^{(a)}$ are the wavenumber of the dilatational wave and the shear wave, respectively. Solutions of Eqs. (8) and (9) can be given as:

$$\Phi^{(a)} = A_1^{(a)}(\alpha,t)e^{-i\beta_d^{(a)}y} + B_1^{(a)}(\alpha,t)e^{i\beta_d^{(a)}y} \tag{10}$$

$$\Psi^{(a)} = A_2^{(a)}(\alpha,t)e^{-i\beta_s^{(a)}y} + B_2^{(a)}(\alpha,t)e^{i\beta_s^{(a)}y} \tag{11}$$

where $\beta_d^{(a)} = \sqrt{[k_d^{(a)}]^2 - \alpha^2}$ and $\beta_s^{(a)} = \sqrt{[k_s^{(a)}]^2 - \alpha^2}$; $A_1^{(a)}(\alpha,t)$ and $B_1^{(a)}(\alpha,t)$ are the potential amplitudes for the positive- and negative-going dilatational waves, respectively; and $A_2^{(a)}(\alpha,t)$ and $B_2^{(a)}(\alpha,t)$ are the potential amplitudes for the positive- and negative-going shear waves, respectively. For 2D plane strain, Eq. (3) can be written as:

$$u_x^{(a)} = \frac{\partial\phi^{(a)}}{\partial x} + \frac{\partial\psi^{(a)}}{\partial y}, \quad u_y^{(a)} = \frac{\partial\phi^{(a)}}{\partial y} - \frac{\partial\psi^{(a)}}{\partial x} \tag{12}$$

The constitutive relationship of Eq. (2) gives the stress components, as:

$$\sigma_{yy}^{(a)} = (\lambda_a + 2\mu_a)\left(\frac{\partial^2\phi^{(a)}}{\partial x^2} + \frac{\partial^2\phi^{(a)}}{\partial y^2}\right) - 2\mu_a\left(\frac{\partial^2\phi^{(a)}}{\partial x^2} + \frac{\partial^2\psi^{(a)}}{\partial x\partial y}\right) \tag{13}$$

$$\sigma_{xy}^{(a)} = \mu_a\left(2\frac{\partial^2\phi^{(a)}}{\partial x\partial y} + \frac{\partial^2\psi^{(a)}}{\partial y^2} - \frac{\partial^2\psi^{(a)}}{\partial x^2}\right) \tag{14}$$

In the wavenumber domain, the displacements ($U_x^{(a)}$, $U_y^{(a)}$) and the stresses ($\Sigma_{yy}^{(\alpha)}$, $\Sigma_{xy}^{(\alpha)}$) can be written in the following forms:

$$U_x^{(a)} = \begin{bmatrix} \alpha\left(A_1^{(a)}(\alpha,t)e^{-i\beta_d^{(a)}y} + B_1^{(a)}(\alpha,t)e^{i\beta_d^{(a)}y}\right) \\ +\beta_s^{(a)}\left(A_2^{(a)}(\alpha,t)e^{-i\beta_s^{(a)}y} - B_2^{(a)}(\alpha,t)e^{i\beta_s^{(a)}y}\right) \end{bmatrix}\cdot(-i) \tag{15}$$

$$U_y^{(a)} = \begin{bmatrix} \beta_d^{(a)}\left(A_1^{(a)}(\alpha,t)e^{-i\beta_d^{(a)}y} - B_1^{(a)}(\alpha,t)e^{i\beta_d^{(a)}y}\right) \\ -\alpha\left(A_2^{(a)}(\alpha,t)e^{-i\beta_s^{(a)}y} + B_2^{(a)}(\alpha,t)e^{i\beta_s^{(a)}y}\right) \end{bmatrix}\cdot(-i) \tag{16}$$

$$\Sigma_{yy}^{(\alpha)} = 2\mu_a\alpha\beta_s^{(a)}\left(A_2^{(a)}(\alpha,t)e^{-i\beta_s^{(a)}y} - B_2^{(a)}(\alpha,t)e^{i\beta_s^{(a)}y}\right) - \left(\lambda_a\alpha^2 + (\lambda_a + 2\mu_a)\left[\beta_d^{(a)}\right]^2\right)\left(A_1^{(a)}(\alpha,t)e^{-i\beta_d^{(a)}y} + B_1^{(a)}(\alpha,t)e^{i\beta_d^{(a)}y}\right) \tag{17}$$

$$\Sigma_{xy}^{(\alpha)} = \begin{bmatrix} \left(\alpha^2 - \left[\beta_s^{(a)}\right]^2\right)\left(A_2^{(a)}(\alpha,t)e^{-i\beta_s^{(a)}y} + B_2^{(a)}(\alpha,t)e^{i\beta_s^{(a)}y}\right) \\ -2\alpha\beta_d^{(a)}\left(A_1^{(a)}(\alpha,t)e^{-i\beta_d^{(a)}y} - B_1^{(a)}(\alpha,t)e^{i\beta_d^{(a)}y}\right) \end{bmatrix}\cdot\mu_a \tag{18}$$

2.2. Acoustic and force excitations

With the two fluids in the upper and lower half-spaces both taken as ideal and inviscid compressible, their motions can be described by the scalar Helmholtz equation in the absence of shear wave, as:

$$\nabla^2 p_i = \frac{1}{c_i^2}\frac{\partial^2 p_i}{\partial t^2} \tag{19}$$

where $i = 1,2$. Applying the Fourier transform pairs of the sound pressure:

$$p_i(x,y,t) = \frac{1}{2\pi}\int_{-\infty}^{+\infty} P_i(\alpha,y,t)e^{-i\alpha x}d\alpha \tag{20}$$

$$P_i(\alpha,y,t) = \int_{-\infty}^{+\infty} p_i(x,y,t)e^{i\alpha x}dx \tag{21}$$

one obtains:

$$\frac{d^2P_i}{dy^2} + \alpha_i^2 P_i = 0 \tag{22}$$

where $\beta_i = \sqrt{k_i^2 - \alpha^2}$, $k_i = \omega/c_i$ being the wavenumber in the i th fluid. The general solution of (22) may be given as:

$$P_i(\alpha,y,t) = A_i(\alpha,t)e^{-i\beta_i y} + B_i(\alpha,t)e^{i\beta_i y} \tag{23}$$

Solutions in the lower and upper half-spaces can be given separately as:

$$P_1(\alpha,y,t) = A_1(\alpha,t)e^{-i\beta_1 y} \tag{24}$$

$$P_2(\alpha,y,t) = B_2(\alpha,t)e^{i\beta_2 y} \tag{25}$$

A line time-harmonic force along the z-direction exerting on the bottom surface of the elastic plate is expressed as:

$$f(x,t) = q_0\delta(x-x_0)e^{i\omega t} \tag{26}$$

where q_0 is the amplitude and x_0 is the location of the force. After Fourier transformation of the line force, it becomes:

$$F(\alpha,t) = q_0 e^{i(\alpha x_0+\omega t)} \tag{27}$$

2.3. Dynamics of rib-stiffeners

Due to the eccentricity between the neutral axis of the stiffeners and the mid-plane of the plate, there actually exists a coupling between the translational and rotational displacements of the stiffeners (Mejdi and Atalla, 2010, 2012). For the case considered in the present study, this eccentricity is much smaller than the other dimensions of the structure, so that for simplicity the coupling effect may be disregarded especially for small displacement vibration (Legault and Atalla, 2010). In the following, the decoupling translational and rotational motions are separately considered.

The classical Timoshenko beam equation is used to model the displacement of the rib-stiffeners in the y-direction (plane strain):

$$\rho A\frac{\partial^2 s_y(x,t)}{\partial t^2} + \frac{\rho^2 I}{G\kappa}\frac{\partial^4 s_y(x,t)}{\partial t^4} = -f_y(x,t) - \frac{\rho I}{GA\kappa}\frac{\partial^2 f_y(x,t)}{\partial t^2} \tag{28}$$

where $s_y(x,t)$ is the rib-stiffener displacement in the y-direction, $f_y(x,t)$ is the force per unit length in the y-direction, ρ is the density, A is the cross-sectional area, I is the second moment of area about the x-axis, G is the shear modulus, and κ is the shear coefficient. The displacement of the rib-stiffener $s_y(x,t)$ has the form:

$$s_y(x,t) = \frac{1}{2\pi}\int_{-\infty}^{+\infty} S_y(\alpha,t)e^{-i\alpha x}d\alpha \tag{29}$$

Therefore, the equivalent force of the rib-stiffener has the same form:

$$f_y(x,t) = \widehat{K}_y\cdot\frac{1}{2\pi}\int_{-\infty}^{+\infty} S_y(\alpha,t)e^{-i\alpha x}d\alpha \tag{30}$$

With perfect bonding between the rib-stiffeners and the elastic plate assumed, the rib-stiffener displacement equals to the plate displacement in the y-direction at the connection $y = h$ ($h = h_t + h_b$). The equivalent force of the rib-stiffener thence becomes:

$$f_y(x,t) = \widehat{K}_y\cdot\frac{1}{2\pi}\int_{-\infty}^{+\infty} U_y^{(b)}(\alpha,h,t)e^{-i\alpha x}d\alpha \tag{31}$$

where

$$\widehat{K}_y = \frac{-\rho A\omega^2 + (\rho^2 I/G\kappa)\omega^4}{-1 + (\rho I/GA\kappa)\omega^2} \tag{32}$$

To model the rotation motion of the rib-stiffener, the torsional wave equation satisfying the plane strain condition is employed:

$$\rho J\frac{\partial^2\theta(x,t)}{\partial t^2} = -m_z(x,t) \tag{33}$$

where $\theta(x,t)$ is the rotational angle of the rib-stiffener about its centroid, $m_z(x,t)$ is the torque per unit length in the z-direction on the top of the rib-stiffener, and J is the polar moment of inertia about the z-axis. The torque can be given by applying the distributed force, as:

$$m_z(x,t) = \left(\frac{h_r}{2}\right)f_x(x,t) \tag{34}$$

where $f_x(x,t)$ is the force per unit length in the x-direction, h_r being the height of the rib-stiffener. The rotation angle can be written in the form:

$$\theta(x,t) = \frac{\partial u_y^{(b)}(x,h,t)}{\partial x} = -\frac{1}{2\pi}\int_{-\infty}^{+\infty} i\alpha U_y^{(b)}(\alpha,h,t)e^{-i\alpha x}d\alpha \tag{35}$$

Thus, the force per unit length has the same form:

$$f_x(x,t) = -\widehat{K}_x\frac{1}{2\pi}\int_{-\infty}^{+\infty} i\alpha U_y^{(b)}(\alpha,h,t)e^{-i\alpha x}d\alpha \tag{36}$$

where

$$\widehat{K}_x = \frac{2J}{h_r}\omega^2\rho \tag{37}$$

2.4. Boundary conditions and solutions

The displacements and stresses of different layers should be continuous at the connected interfaces, which ensure the sole solution of the vibroacoustic system. At the three interfaces ($y = 0$, h_t and $h = h_t + h_b$), there are ten boundary conditions that the displacements and stresses should obey:

$$\sigma_{yy}^{(t)}\Big|_{y=h_t} = \sigma_{yy}^{(b)}\Big|_{y=h_t},\quad \sigma_{xy}^{(t)}\Big|_{y=h_t} = \sigma_{xy}^{(b)}\Big|_{y=h_t} \tag{38}$$

$$u_x^{(t)}\Big|_{y=h_t} = u_x^{(b)}\Big|_{y=h_t},\quad u_y^{(t)}\Big|_{y=h_t} = u_y^{(b)}\Big|_{y=h_t} \tag{39}$$

$$\rho_2\frac{\partial^2 u_y^{(t)}}{\partial t^2}\Big|_{y=0} = -\frac{\partial p_2}{\partial y}\Big|_{y=0},\quad \rho_1\frac{\partial^2 u_y^{(b)}}{\partial t^2}\Big|_{y=h} = -\frac{\partial p_1}{\partial y}\Big|_{y=h} \tag{40}$$

$$\sigma_{yy}^{(t)}\Big|_{y=0} = -p_2|_{y=0},\quad \sigma_{xy}^{(t)}\Big|_{y=0} = 0 \tag{41}$$

$$\sigma_{yy}^{(b)}\Big|_{y=h} = -(p_1+f)|_{y=h} + \sum_{n=-\infty}^{+\infty} f_y(x,t)\delta(x-nL),\quad \sigma_{xy}^{(b)}\Big|_{y=h} = \sum_{n=-\infty}^{+\infty} f_x(x,t)\delta(x-nL) \tag{42}$$

Here, the discretely distributed stiffeners (or the offset distances between the z-axis and the centroid of the stiffeners) have been accurately considered via the application of the Dirac delta function $\delta(x-nL)$, if one notices that $\delta(x-nL) = 1$ holds only at the stiffener locations $x = 0,\pm L,\pm 2L$ ….

Substituting the expressions of the displacements and stresses in the wavenumber domain into the above boundary conditions and applying the identity:

$$\sum_{n=-\infty}^{+\infty}\delta(x-nL)=\frac{1}{L}\sum_{n=-\infty}^{+\infty}e^{-i2n\pi x/L} \tag{43}$$

one obtains the following ten equations for the vibroacoustic system of Fig. 1:

$$\begin{bmatrix}2\mu_t\alpha\beta_s^{(t)}\left(A_2^{(t)}(\alpha,t)e^{-i\beta_s^{(t)}h_t}-B_2^{(t)}(\alpha,t)e^{i\beta_s^{(t)}h_t}\right)\\-\left(\lambda_t\alpha^2+(\lambda_t+2\mu_t)\left[\beta_d^{(t)}\right]^2\right)\left(A_1^{(t)}(\alpha,t)e^{-i\beta_d^{(t)}h_t}+B_1^{(t)}(\alpha,t)e^{i\beta_d^{(t)}h_t}\right)\end{bmatrix}$$
$$-\begin{bmatrix}2\mu_b\alpha\beta_s^{(b)}\left(A_2^{(b)}(\alpha,t)e^{-i\beta_s^{(b)}h_t}-B_2^{(b)}(\alpha,t)e^{i\beta_s^{(b)}h_t}\right)\\-\left(\lambda_b\alpha^2+(\lambda_b+2\mu_b)\left[\beta_d^{(b)}\right]^2\right)\left(A_1^{(b)}(\alpha,t)e^{-i\beta_d^{(b)}h_t}+B_1^{(b)}(\alpha,t)e^{i\beta_d^{(b)}h_t}\right)\end{bmatrix}$$
$$=0 \tag{44}$$

$$\begin{bmatrix}\left(\alpha^2-\left[\beta_s^{(t)}\right]^2\right)\left(A_2^{(t)}(\alpha,t)e^{-i\beta_s^{(t)}h_t}+B_2^{(t)}(\alpha,t)e^{i\beta_s^{(t)}h_t}\right)\\-2\alpha\beta_d^{(t)}\left(A_1^{(t)}(\alpha,t)e^{-i\beta_d^{(t)}h_t}-B_1^{(t)}(\alpha,t)e^{i\beta_d^{(t)}h_t}\right)\end{bmatrix}\cdot\mu_t$$
$$-\begin{bmatrix}\left(\alpha^2-\left[\beta_s^{(b)}\right]^2\right)\left(A_2^{(b)}(\alpha,t)e^{-i\beta_s^{(b)}h_t}+B_2^{(b)}(\alpha,t)e^{i\beta_s^{(b)}h_t}\right)\\-2\alpha\beta_d^{(b)}\left(A_1^{(b)}(\alpha,t)e^{-i\beta_d^{(b)}h_t}-B_1^{(b)}(\alpha,t)e^{i\beta_d^{(b)}h_t}\right)\end{bmatrix}\cdot\mu_b$$
$$=0 \tag{45}$$

$$\left[\alpha\left(A_1^{(t)}(\alpha,t)e^{-i\beta_d^{(t)}h_t}+B_1^{(t)}(\alpha,t)e^{i\beta_d^{(t)}h_t}\right)+\beta_s^{(t)}\left(A_2^{(t)}(\alpha,t)e^{-i\beta_s^{(t)}h_t}\right.\right.$$
$$\left.-B_2^{(t)}(\alpha,t)e^{i\beta_s^{(t)}h_t}\right)\Big]-\Big[\alpha\left(A_1^{(b)}(\alpha,t)e^{-i\beta_d^{(b)}h_t}+B_1^{(b)}(\alpha,t)e^{i\beta_d^{(b)}h_t}\right)$$
$$+\beta_s^{(b)}\left(A_2^{(b)}(\alpha,t)e^{-i\beta_s^{(b)}h_t}-B_2^{(b)}(\alpha,t)e^{i\beta_s^{(b)}h_t}\right)\Big]$$
$$=0 \tag{46}$$

$$\left[\beta_d^{(t)}\left(A_1^{(t)}(\alpha,t)e^{-i\beta_d^{(t)}h_t}-B_1^{(t)}(\alpha,t)e^{i\beta_d^{(t)}h_t}\right)-\alpha\left(A_2^{(t)}(\alpha,t)e^{-i\beta_s^{(t)}h_t}\right.\right.$$
$$\left.+B_2^{(t)}(\alpha,t)e^{i\beta_s^{(t)}h_t}\right)\Big]-\Big[\beta_d^{(b)}\left(A_1^{(b)}(\alpha,t)e^{-i\beta_d^{(b)}h_t}-B_1^{(b)}(\alpha,t)e^{i\beta_d^{(b)}h_t}\right)$$
$$-\alpha\left(A_2^{(b)}(\alpha,t)e^{-i\beta_s^{(b)}h_t}+B_2^{(b)}(\alpha,t)e^{i\beta_s^{(b)}h_t}\right)\Big]$$
$$=0 \tag{47}$$

$$\rho_2\omega^2\left[\beta_d^{(t)}\left(A_1^{(t)}(\alpha,t)-B_1^{(t)}(\alpha,t)\right)-\alpha\left(A_2^{(t)}(\alpha,t)+B_2^{(t)}(\alpha,t)\right)\right]$$
$$=-\alpha_2B_2(\alpha,t) \tag{48}$$

$$\rho_1\omega^2\left[\beta_d^{(b)}\left(A_1^{(b)}(\alpha,t)e^{-i\beta_d^{(b)}h}-B_1^{(b)}(\alpha,t)e^{i\beta_d^{(b)}h}\right)-\alpha\left(A_2^{(b)}(\alpha,t)e^{-i\beta_s^{(b)}h}\right.\right.$$
$$\left.+B_2^{(b)}(\alpha,t)e^{i\beta_s^{(b)}h}\right)\Big]$$
$$=\alpha_1A_1(\alpha,t)e^{-i\alpha_1h} \tag{49}$$

$$2\mu_t\alpha\beta_s^{(t)}\left(A_2^{(t)}(\alpha,t)-B_2^{(t)}(\alpha,t)\right)-\left(\lambda_t\alpha^2+(\lambda_t+2\mu_t)\left[\beta_d^{(t)}\right]^2\right)$$
$$\times\left(A_1^{(t)}(\alpha,t)+B_1^{(t)}(\alpha,t)\right)$$
$$=-B_2(\alpha,t) \tag{50}$$

$$\left[\left(\alpha^2-\left[\beta_s^{(t)}\right]^2\right)\left(A_2^{(t)}(\alpha,t)+B_2^{(t)}(\alpha,t)\right)-2\alpha\beta_d^{(t)}\left(A_1^{(t)}(\alpha,t)\right.\right.$$
$$\left.-B_1^{(t)}(\alpha,t)\right)\Big]\cdot\mu_t$$
$$=0 \tag{51}$$

$$2\mu_b\alpha\beta_s^{(b)}\left(A_2^{(b)}(\alpha,t)e^{-i\beta_s^{(b)}h}-B_2^{(b)}(\alpha,t)e^{i\beta_s^{(b)}h}\right)-\left(\lambda_b\alpha^2\right.$$
$$\left.+(\lambda_b+2\mu_b)\left[\beta_d^{(b)}\right]^2\right)\left(A_1^{(b)}(\alpha,t)e^{-i\beta_d^{(b)}h}+B_1^{(b)}(\alpha,t)e^{i\beta_d^{(b)}h}\right)$$
$$=-\left(A_1(\alpha,t)e^{-i\alpha_1h}+q_0e^{i(\alpha x_0+\omega t)}\right)+\frac{\widehat{K}_y}{L}\sum_{n=-\infty}^{+\infty}U_y^{(b)}(\alpha_n,h,t) \tag{52}$$

$$\begin{bmatrix}\left(\alpha^2-\left[\beta_s^{(b)}\right]^2\right)\left(A_2^{(b)}(\alpha,t)e^{-i\beta_s^{(b)}h}+B_2^{(b)}(\alpha,t)e^{i\beta_s^{(b)}h}\right)\\-2\alpha\beta_d^{(b)}\left(A_1^{(b)}(\alpha,t)e^{-i\beta_d^{(b)}h}-B_1^{(b)}(\alpha,t)e^{i\beta_d^{(b)}h}\right)\end{bmatrix}\cdot\mu_b$$
$$=-\frac{\widehat{K}_x}{L}\sum_{n=-\infty}^{+\infty}i\alpha_nU_y^{(b)}(\alpha_n,h,t) \tag{53}$$

Here, $\alpha_n=\alpha-2n\pi/L$, and the displacement of the bottom surface of the elastic plate, $U_y^{(b)}(\alpha,h,t)$, is given by:

$$U_y^{(b)}(\alpha,h,t)=(-i)\cdot\left[\beta_d^{(b)}\left(A_1^{(b)}(\alpha,t)e^{-i\beta_d^{(b)}h}-B_1^{(b)}(\alpha,t)e^{i\beta_d^{(b)}h}\right)\right.$$
$$\left.-\alpha\left(A_2^{(b)}(\alpha,t)e^{-i\beta_s^{(b)}h}+B_2^{(b)}(\alpha,t)e^{i\beta_s^{(b)}h}\right)\right] \tag{54}$$

The ten unknown wave propagation coefficients form a vector $\{X_n\}$, as:

$$\{X_n\}=\left\{\begin{matrix}A_1^{(t)}(\alpha_n) & B_1^{(t)}(\alpha_n) & A_2^{(t)}(\alpha_n) & B_2^{(t)}(\alpha_n) & A_1^{(b)}(\alpha_n) & B_1^{(b)}(\alpha_n)\\ & A_2^{(b)}(\alpha_n) & B_2^{(b)}(\alpha_n) & A_1(\alpha_n) & B_2(\alpha_n) & \end{matrix}\right\}^T \tag{55}$$

For simplicity, the ten boundary value equations can be rewritten in matrix form, as:

$$[T(\alpha)]\{X\}=\sum_{n=-\infty}^{+\infty}[U(\alpha_n)]\{X_n\}+\{F(\alpha)\} \tag{56}$$

where $[T(\alpha)]$ is a 10×10 matrix that describes the dynamic motions of the coating layer and the elastic plate, $\{X_n\}$ is the 10×1 vector of unknown wave propagation coefficients, $[U(\alpha_n)]$ is the 10×10 matrix that models the equivalent rib-stiffener forces exerting on the elastic plate, and $\{F(\alpha)\}$ is the 10×1 vector that represents the line force excitation. For convenience, Eq. (56) can be further written in a global matrix notation as:

$$\widehat{T}\widehat{X}=\widehat{U}\widehat{X}+\widehat{F} \tag{57}$$

where $\widehat{T}$ is a block diagonal matrix in the form:

$$\widehat{\mathrm{T}} = \begin{bmatrix} \ddots & & \vdots & & \iddots \\ & \mathrm{T}(\alpha_{-1}) & 0 & 0 & \\ \cdots & 0 & \mathrm{T}(\alpha) & 0 & \cdots \\ & 0 & 0 & \mathrm{T}(\alpha_1) & \\ \iddots & & \vdots & & \ddots \end{bmatrix}; \tag{58}$$

$\widehat{\mathrm{U}}$ is a rank block matrix:

$$\widehat{\mathrm{U}} = \begin{bmatrix} \ddots & & \vdots & & \iddots \\ & \mathrm{U}(\alpha_{-1}) & \mathrm{U}(\alpha) & \mathrm{U}(\alpha_1) & \\ \cdots & \mathrm{U}(\alpha_{-1}) & \mathrm{U}(\alpha) & \mathrm{U}(\alpha_1) & \cdots \\ & \mathrm{U}(\alpha_{-1}) & \mathrm{U}(\alpha) & \mathrm{U}(\alpha_1) & \\ \iddots & & \vdots & & \ddots \end{bmatrix}; \tag{59}$$

$\widehat{\mathrm{X}}$ is the vector for unknown wave propagation coefficients:

$$\widehat{\mathrm{X}} = \begin{bmatrix} \cdots & \{\mathrm{X}_{-1}\}^{\mathrm{T}} & \{\mathrm{X}_0\}^{\mathrm{T}} & \{\mathrm{X}_1\}^{\mathrm{T}} & \cdots \end{bmatrix}^{\mathrm{T}} \tag{60}$$

and $\widehat{\mathrm{F}}$ is the line force excitation vector:

$$\widehat{\mathrm{F}} = \begin{bmatrix} \cdots & \{\mathrm{F}_{-1}\}^{\mathrm{T}} & \{\mathrm{F}_0\}^{\mathrm{T}} & \{\mathrm{F}_1\}^{\mathrm{T}} & \cdots \end{bmatrix}^{\mathrm{T}} \tag{61}$$

The 0 term in (58) represents a 10×10 matrix with all zero entries. The unknown wave propagation coefficients can be obtained by solving the equation:

$$\widehat{\mathrm{X}} = \left[\widehat{\mathrm{T}} - \widehat{\mathrm{U}}\right]^{-1} \widehat{\mathrm{F}} \tag{62}$$

Once the wave propagation coefficients are determined, the near field radiated sound pressure can be expressed as:

$$p_2(x,y) = \frac{\rho_2 \omega^2}{2\pi} \int_{-\infty}^{+\infty} \frac{U_y^{(t)}(\alpha,0)}{i\beta_2} e^{-i\alpha x + i\beta_2 y} d\alpha \tag{63}$$

while the far field radiated sound pressure can be determined by (Mace, 1981; Xin and Lu, 2010b)

$$p_2(r,\theta) = -\rho_2 \omega^2 U_y^{(t)}(k_2 \sin\theta, 0) e^{ik_2 r} \Big/ 2\pi r \tag{64}$$

where θ is the radiated angle with respect to the y-axis (Fig. 1).

To evaluate the extent of noise reduction achieved by adding a compliant coating layer to the structure, the dimensionless indictor NR is defined as the ratio of sound pressure at the measuring point without and with attaching the compliant coating layer in decibel scale, i.e.:

$$NR = 20 \log_{10} \left(\frac{p_2(r,\theta)|_{h_t=0}}{p_2(r,\theta)|_{h_t=h_t}} \right) \tag{65}$$

3. Numerical results and discussion

Numerical calculations are conducted in this section to examine the noise reduction behavior of a compliant coating layer affixed to a periodically rib-stiffened plate structure. The two cases of the structure immersed in air-air and air-water (i.e., fluid 1-fluid 2) are separately considered. Unless otherwise specified, the far field radiated sound pressure at the measuring point (0, −1, 0) m is applied to calculate the noise reduction. Structural dimensions and material properties employed in numerical calculation are listed in Table 1. Sound pressure levels (SPL) of the rib-stiffened plate without and with the compliant coating layer, as well as noise reduction of the coating layer are firstly analyzed. Subsequently, the effects of the compliant coating layer thickness, radiation angle, coating material properties and excitation location on SPL are quantified.

Table 1
Structural dimensions and material properties.

Description	Parameter & Value
Decoupling coating layer	
Thickness	$h_t = 40$ mm
Lamé constant	$\lambda_t = 28.1$ MPa
Lamé constant	$\mu_t = 9.7$ MPa
Density	$\rho_t = 600$ kg/m^3
Elastic plate	
Thickness	$h_b = 10$ mm
Lamé constant	$\lambda_b = 51.1$ GPa
Lamé constant	$\mu_t = 26.3$ GPa
Density	$\rho_t = 2710$ kg/m^3
Rib-stiffeners	
Thickness	$t = 20$ mm
Height	$h_r = 50$ mm
Spacing	$L = 0.5$ m
Young's modulus	$E = 70$ GPa
Density	$\rho = 2710$ kg/m^3
Poisson ratio	$\nu = 0.33$
Shear coefficient	$\kappa = 0.833$
Fluid 1 (air)	
Density	$\rho_f = 1.21$ kg/m^3
Sound speed	$c_f = 343$ m/s
Fluid 2 (water)	
Density	$\rho_f = 1025$ kg/m^3
Sound speed	$c_f = 1475$ m/s

3.1. Sound radiation and noise reduction

Using the theoretical model established in the previous section, we first calculate the far field radiated sound pressure of the rib-stiffened plate without and with a compliant coating layer attached, for both the air-air and air-water cases. The noise reduction performance of the coating can thence be obtained and intuitively understood, as shown in Figs. 2 and 3. When no coating is attached, several resonant peaks and dips appear in the SPL curve for the rib-stiffened plate in the air-air case, but these resonant peaks and dips disappear in the counterpart curve of the air-water case. The latter is attributed to the heavy fluid loading effect. In comparison, when the rib-stiffened plate is covered with a coating layer, a variety of resonant peaks and dips emerge in both the air-air and the air-water cases. These newly emerged peaks and dips are caused by the waveguide behavior of the relatively soft coating layer (Keltie, 1998). Namely, the boundary conditions restrict the fluid 2/coating/plate system to constitute a rigid-rigid dilatational waveguide model and a rigid-free shear waveguide model, which correspond to the resonant dips and peaks in the SPL curves, respectively. Also, the coating layer affixed to the rib-stiffened plate introduces complicated wave interaction among the dilatational and shear waves in the coating layer and the elastic plate as well as the flexural waves in the rib-stiffeners, which should contribute to some of the peaks and dips in the SPL curves. Moreover, the SPL curve of the air-air case (Fig. 2) exhibits much denser peaks and dips than that of the air-water case (Fig. 3), owing to the more pronounced added-mass effect of the heavy fluid loading.

Since the far field sound pressures are known for both the without and with coating cases, the noise reduction achieved by the coating layer is actually the difference of the two pressures in decibel scale. As shown in Figs. 2 and 3, the noise reduction of the coating in the air-water case is several tens of decibels larger in average and exhibits relatively sparser peaks and dips than that in

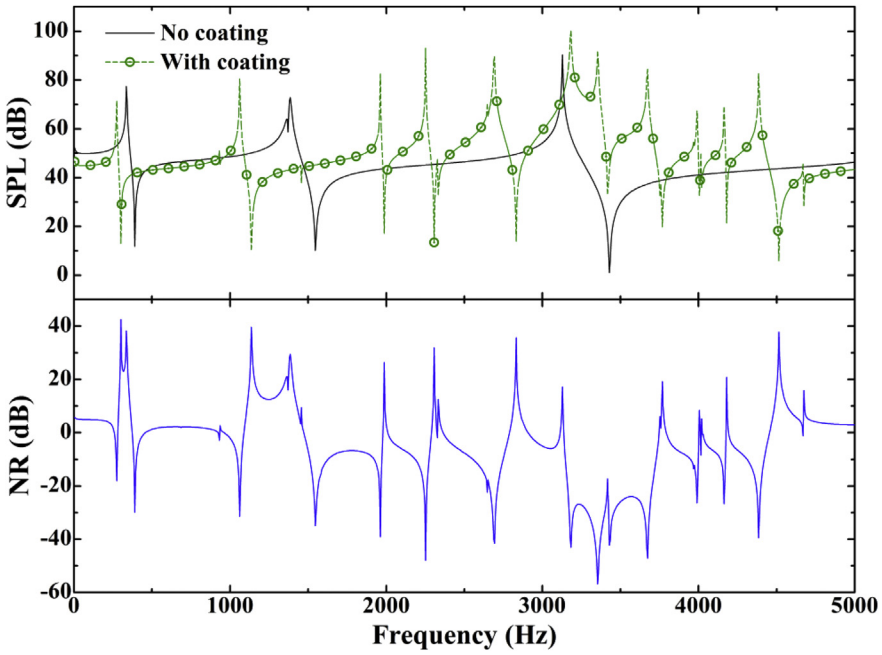

Fig. 2. Noise reduction achieved by affixing a compliant coating layer to a periodically rib-stiffened plate in air-air case.

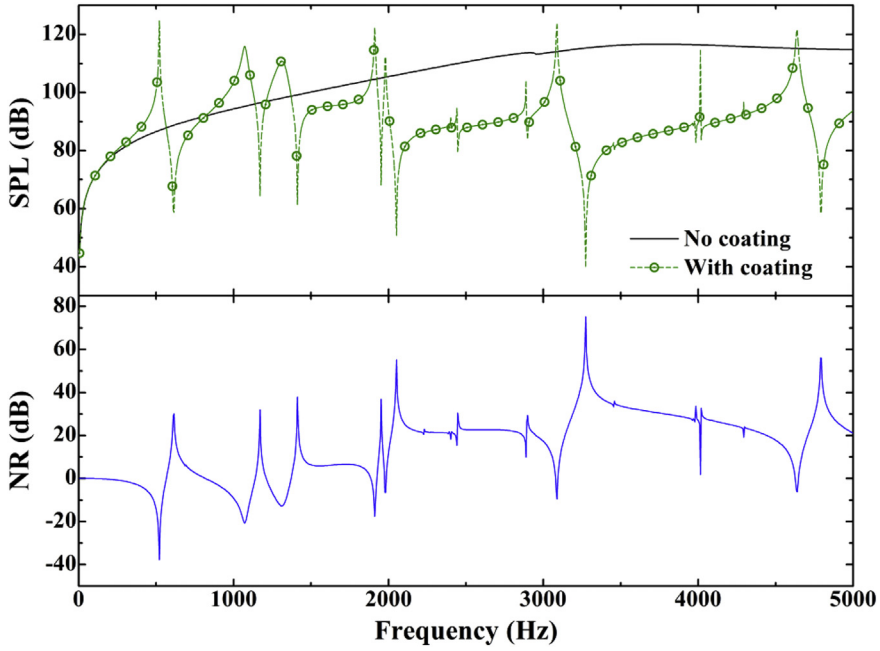

Fig. 3. Noise reduction achieved by affixing a compliant coating layer to a periodically rib-stiffened plate in air-water case.

the air-air case. These results demonstrate the significant difference between heavy fluid loading (water) and light fluid loading (air).

3.2. *Effect of compliant coating thickness*

The influence of coating thickness on its noise reduction capability is studied by varying the coating thickness while keeping all the other parameters unchanged. Selected results are presented in Figs. 4 and 5 for the air-air and air-water cases, respectively. As the coating thickness is increased, the resonant peaks and dips mainly move to lower frequencies, except that several peaks and dips caused by the rib-stiffened plate itself hold on their original sites. This trend is particularly obvious in the air-water case (Fig. 5). Because the heavy fluid loading significantly suppresses the resonance of the rib-stiffened plate itself (see Fig. 3), the remaining peaks and dips are mainly related to the dilatational waveguide and shear waveguide behaviors of the fluid 2/coating/plate coupling system. These waveguide behaviors are closely associated with the coating thickness, causing the shift of the peaks and dips to lower frequencies in Fig. 5. In contrast, to a large extent, the complicated wave interaction in the air-air case overwhelms the shift of the waveguide-induced peaks and dips to lower frequencies.

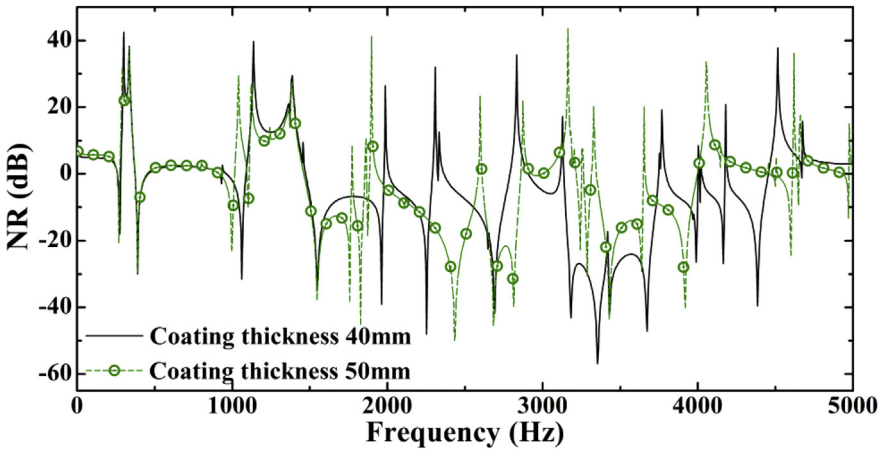

Fig. 4. Noise reduction achieved by affixing a compliant coating layer to a periodically rib-stiffened plate in air-air case: effect of coating thickness.

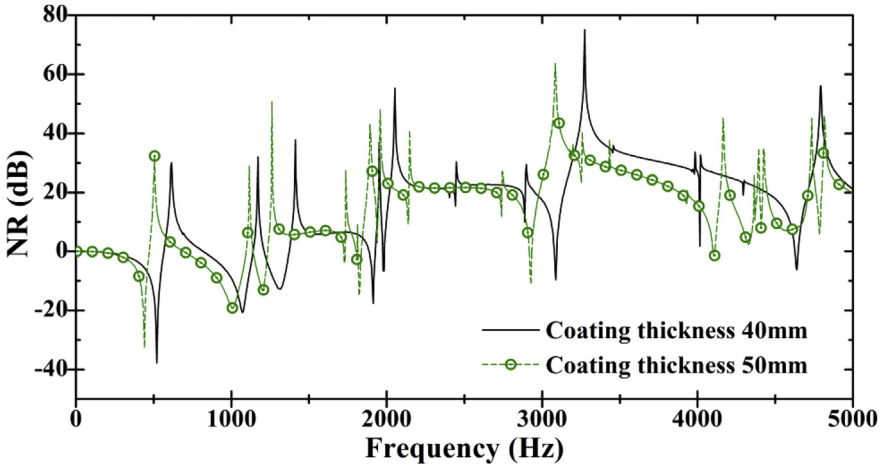

Fig. 5. Noise reduction achieved by affixing a compliant coating layer to a periodically rib-stiffened plate in air-water case: effect of coating thickness.

3.3. *Effect of radiation angle*

As shown in Figs. 6 and 7 for both the air-air and air-water cases, the noise reduction characteristics of the coating layer in different radiation angle directions are explored by comparing the two typical radiation angles of 0° and 45°. When the radiation angle is changed from 0° to 45°, the averaged noise reduction scale remains almost unchanged. However, there is a significant shift of the peaks and dips towards lower frequencies, which is especially obvious in the air-air case (Fig. 6). The waveguide behaviors of the coating

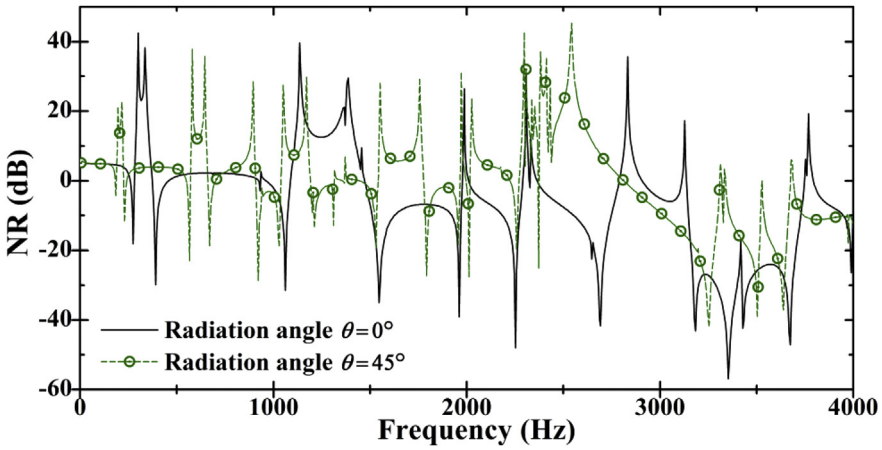

Fig. 6. Noise reduction achieved by affixing a compliant coating layer to a periodically rib-stiffened plate in air-air case: effect of radiation angle.

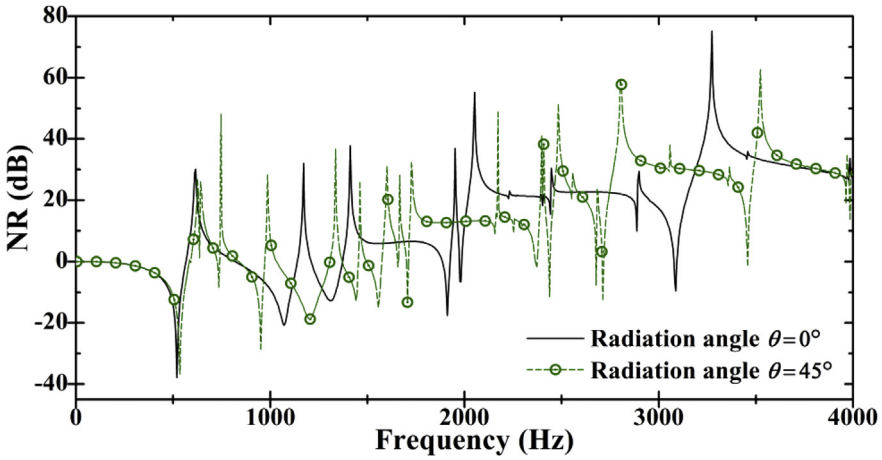

Fig. 7. Noise reduction achieved by affixing a compliant coating layer to a periodically rib-stiffened plate in air-water case: effect of radiation angle.

layer, the resonant mode of the rib-stiffened plate itself, and the complicated wave interactions combine to induce the maximum and minimum values of the normal velocity of the radiating surface. A superposition of these contributes to the far field sound pressure at the measuring point; see Eqs. (63) and (64). Therefore, the radiated sound pressure and noise reduction are closely related to the direction of the measuring point (i.e., the radiation angle; see Eq. (64)). The only exception is that the first dip in Fig. 7 moves, albeit slightly, to a higher frequency when the radiation angle is changed from 0° to 45°. As this dip is associated with the mass-spring-mass mode constituted by the fluid 2/coating/plate system, it does not follow the trend of the other resonant modes. Note that the mass-spring-mass mode does not exist in the air-air case (Fig. 6), since the light fluid (air) cannot be regarded as an effective lumped mass.

3.4. Effect of coating material properties

When a coating layer is used to reduce the sound radiation of elastic structures, its properties should affect the noise reduction behavior of the coating itself. To evaluate the effect of coating material properties on noise reduction, the dilatational wave speed and the shear wave speed of the coating material are selected. Corresponding results for the air-air case are presented in Figs. 8 and 9, which show that altering the dilatational wave and shear wave speeds of the coating material does not significantly affect the tendency of the noise reduction curves. Only the peaks and dips associated with the waveguide modes of the coating layer move, while those associated with the modes of the rib-stiffened plate itself almost remain unchanged. Because the coating layer is much stiffer than air, alterations of the dilatational wave and shear wave speeds as considered here does not significantly change the stiffness of the relatively stiff coating layer.

However, in the presence of a heavy fluid (water), the coating layer may be regarded as a relatively soft material. In this case, as shown in Figs. 10 and 11, changing either the dilatational wave speed or shear wave speed of the coating material induces remarkable stiffness change of the coating, causing therefore significant alterations of its noise reduction behavior. As the dilatational (or shear) wave speed is increased, the peaks and dips associated with the waveguide modes of the coating all shift towards high frequencies. Similar to Fig. 7, the mass-spring-mass mode in Fig. 10 does not follow the same trend as others.

The results presented here suggest that, by changing the material properties of the coating layer, it is feasible to noticeably improve its noise reduction performance in specific frequency ranges.

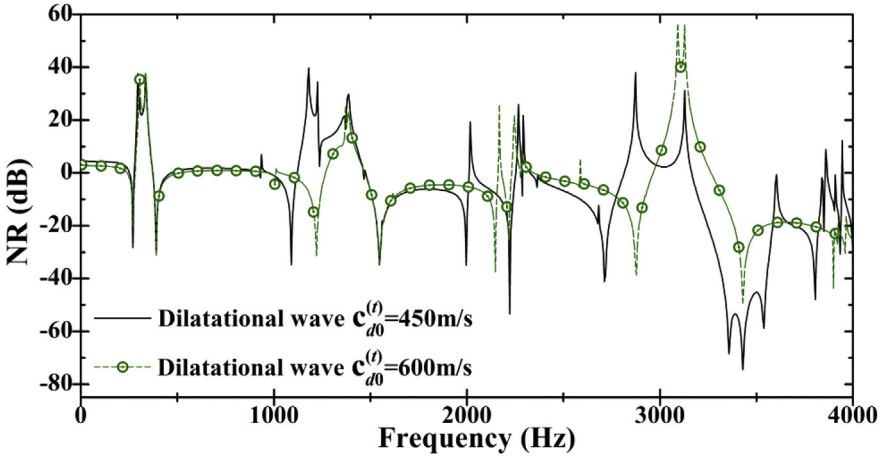

Fig. 8. Noise reduction achieved by affixing a compliant coating layer to a periodically rib-stiffened plate in air-air case: effect of dilatational wave speed.

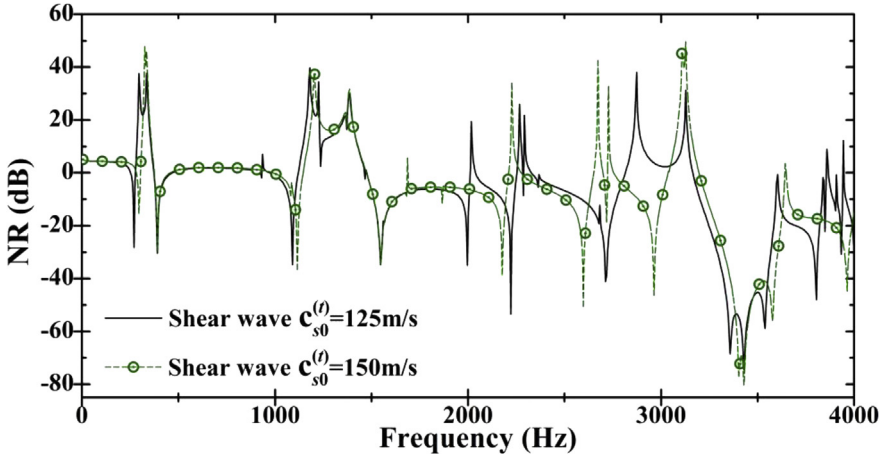

Fig. 9. Noise reduction achieved by affixing a compliant coating layer to a periodically rib-stiffened plate in air-air case: effect of shear wave speed.

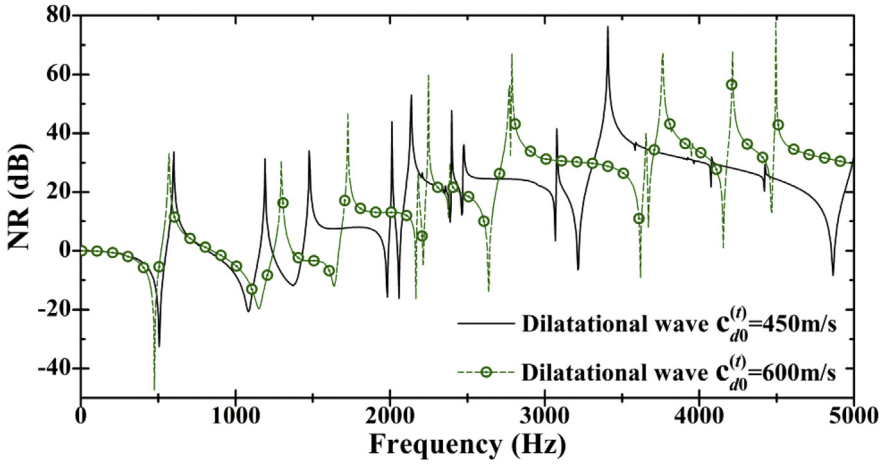

Fig. 10. Noise reduction achieved by affixing a compliant coating layer to a periodically rib-stiffened plate in air-water case: effect of dilatational wave speed.

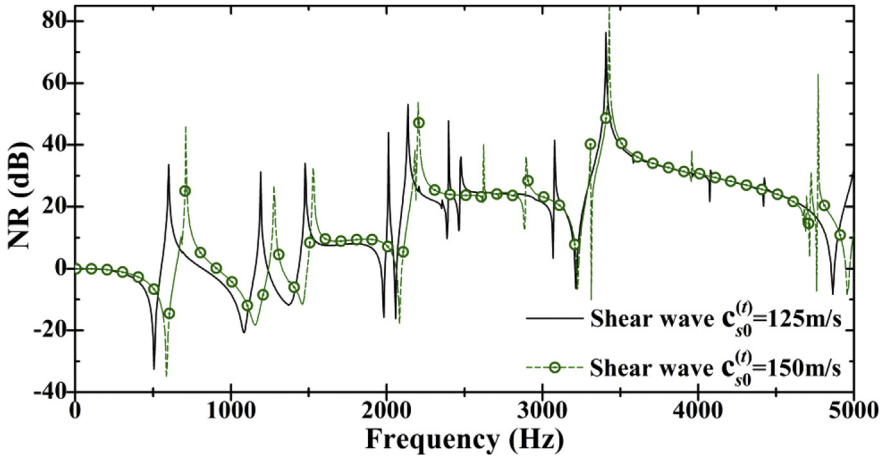

Fig. 11. Noise reduction achieved by affixing a compliant coating layer to a periodically rib-stiffened plate in air-water case: effect of shear wave speed.

3.5. *Effect of excitation location*

Since the elastic plate is periodically attached with rib-stiffeners (Fig. 1), two typical excitation locations of $x_0 = 0$ and $x_0 = L/2$ are chosen to examine the effect of excitation location on noise reduction of the coating. Other relevant parameters remain unchanged in the theoretical model. Notice that, with reference to the selected coordinate system of Fig. 1, these two locations mean that the line force is exerted on the center of two adjacent rib-stiffeners and the right side of one rib-stiffener, respectively. Again, both the

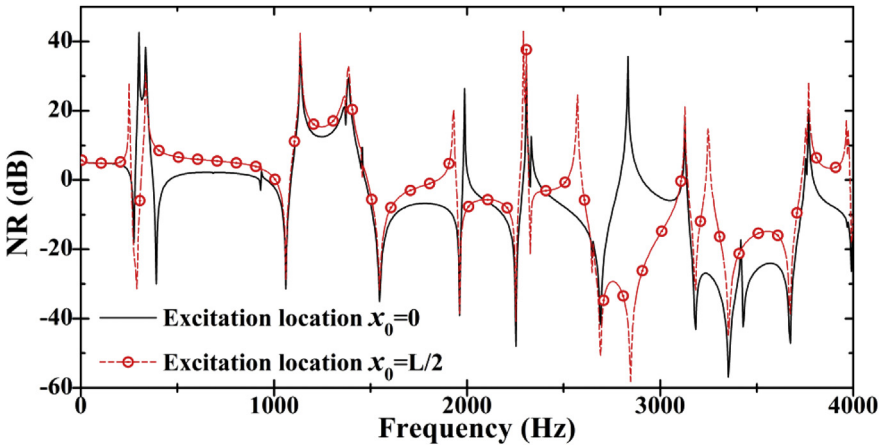

Fig. 12. Noise reduction achieved by affixing a compliant coating layer to a periodically rib-stiffened plate in air-air case: effect of excitation location.

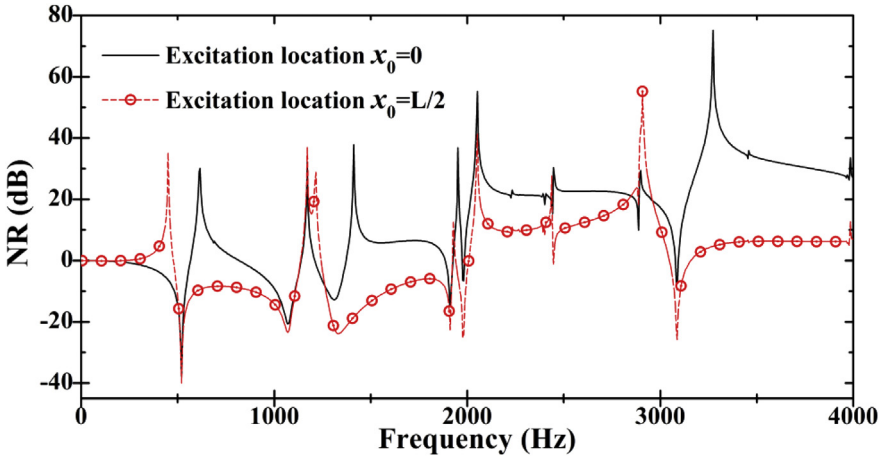

Fig. 13. Noise reduction achieved by affixing a compliant coating layer to a periodically rib-stiffened plate in air-water case: effect of excitation location.

air-air and air-water cases are considered.

For the air-air case, when the excitation location is altered from 0 to $L/2$, it can be seen from Fig. 12 that noise reduction increases over a wide frequency range except the range between approximately 2700 Hz–3200 Hz. In comparison, for the air-water case shown in Fig. 13, the noise reduction significantly decreases when the excitation location is changed from 0 to $L/2$, except for several individual peaks. By comparing the results of Figs. 12 and 13, it is seen that the noise reduction behavior of the coating layer is much more sensitive to excitation location in the air-water case than that in the air-air case. In other words, in underwater environment, excitation directly exerted on the rib-stiffener of the present structure can dramatically destruct the noise reduction performance of the coating layer.

4. Conclusions

An elasticity model is established to investigate the noise reduction performance of a compliant coating layer affixed to a periodically rib-stiffened elastic plate. The structure is immersed in two different inviscid fluids so as to accurately mimic the interior and exterior fluid media of the structure in underwater environment. The theory of plane strain elasticity is adopted to model the dilatational and shear motion behaviors of the coating layer and the elastic plate. Motions of the inviscid fluids are described using the scalar Helmholtz equation in the absence of shear wave, while motions of the rib-stiffeners are characterized by employing the Timoshenko beam equation and the torsional equation. As a vibroacoustic coupling system, the fluid loadings and the forces of the rib-stiffeners are coupled with the vibration of the coating layer and the plate by enforcing displacement and stress continuity conditions. Solution of the unknown wave propagation coefficients in the final system of governing equations enables the noise reduction analysis. Based upon the proposed theoretical model, numerical calculations are performed to investigate the effects of coating thickness, coating material properties, radiation angle, and excitation location on the noise reduction performance of the coating layer.

The results demonstrate that heavy fluid loading (e.g., water) is able to suppress the resonance behavior of periodically rib-stiffened plates, so that the waveguide behaviors of the coating prevail in the air-water case. Increasing the coating thickness shifts the resonant peaks and dips associated with the waveguide behavior of the coating towards lower frequencies, while those arising from the resonant mode of the rib-stiffened plate remain unchanged. Increasing the radiation angle also shifts the peaks and dips to lower frequencies, except for the mass-spring-mass resonance peak that is almost unchanged. Increasing the dilatational and shear wave speeds of the coating material leads to slight changes of the resonant peaks and dips related to the rib-stiffened

plate and noticeable shifting to higher frequencies of the peaks and dips associated with the waveguide behavior of the coating. Relative to exciting at the center of two adjacent rib-stiffeners, excitation exerted directly on the rib-stiffener can obviously deteriorate the noise reduction performance of the coating layer. The noise reduction behavior of the coating is more sensitive to changes in system parameters in the air-water case than that in the air-air case. The theoretical results presented in this study provide valuable guidance on experimental research and structural design related to decoupling coating layers affixed to underwater elastic structures. Future research needs to consider the combined mechanical and acoustical behavior of rib-stiffened structures attached with an anechoic coating for underwater engineering applications.

Acknowledgements

This work was supported by the National Natural Science Foundation of China (51528501) and the Fundamental Research Funds for Central Universities (2014qngz12).

Appendix A. Derivation of equation (56)

The nonzero entries of [T(α)] matrix are:

$$\begin{aligned}
T_{1,1} &= -\left(\lambda_t\alpha^2 + (\lambda_t+2\mu_t)\left[\beta_d^{(t)}\right]^2\right)e^{-i\beta_d^{(t)}h_t}\\
T_{1,2} &= -\left(\lambda_t\alpha^2 + (\lambda_t+2\mu_t)\left[\beta_d^{(t)}\right]^2\right)e^{i\beta_d^{(t)}h_t}\\
T_{1,3} &= 2\mu_t\alpha\beta_s^{(t)}e^{-i\beta_s^{(t)}h_t}\\
T_{1,4} &= -2\mu_t\alpha\beta_s^{(t)}e^{i\beta_s^{(t)}h_t}\\
T_{1,5} &= \left(\lambda_b\alpha^2 + (\lambda_b+2\mu_b)\left[\beta_d^{(b)}\right]^2\right)e^{-i\beta_d^{(b)}h_t}\\
T_{1,6} &= \left(\lambda_b\alpha^2 + (\lambda_b+2\mu_b)\left[\beta_d^{(b)}\right]^2\right)e^{i\beta_d^{(b)}h_t}\\
T_{1,7} &= -2\mu_b\alpha\beta_s^{(b)}e^{-i\beta_s^{(b)}h_t}\\
T_{1,8} &= 2\mu_b\alpha\beta_s^{(b)}e^{i\beta_s^{(b)}h_t}
\end{aligned} \tag{A1}$$

$$\begin{aligned}
T_{2,1} &= -2\mu_t\alpha\beta_d^{(t)}e^{-i\beta_d^{(t)}h_t}\\
T_{2,2} &= 2\mu_t\alpha\beta_d^{(t)}e^{i\beta_d^{(t)}h_t}\\
T_{2,3} &= \mu_t\left(\alpha^2 - \left[\beta_s^{(t)}\right]^2\right)e^{-i\beta_s^{(t)}h_t}\\
T_{2,4} &= \mu_t\left(\alpha^2 - \left[\beta_s^{(t)}\right]^2\right)e^{i\beta_s^{(t)}h_t}\\
T_{2,5} &= 2\mu_b\alpha\beta_d^{(b)}e^{-i\beta_d^{(b)}h_t}\\
T_{2,6} &= -2\mu_b\alpha\beta_d^{(b)}e^{i\beta_d^{(b)}h_t}\\
T_{2,7} &= -\mu_b\left(\alpha^2 - \left[\beta_s^{(b)}\right]^2\right)e^{-i\beta_s^{(b)}h_t}\\
T_{2,8} &= -\mu_b\left(\alpha^2 - \left[\beta_s^{(b)}\right]^2\right)e^{i\beta_s^{(b)}h_t}
\end{aligned} \tag{A2}$$

$$\begin{aligned}
T_{3,1} &= \alpha e^{-i\beta_d^{(t)}h_t}\\
T_{3,2} &= \alpha e^{i\beta_d^{(t)}h_t}\\
T_{3,3} &= \beta_s^{(t)}e^{-i\beta_s^{(t)}h_t}\\
T_{3,4} &= -\beta_s^{(t)}e^{i\beta_s^{(t)}h_t}\\
T_{3,5} &= -\alpha e^{-i\beta_d^{(b)}h_t}\\
T_{3,6} &= -\alpha e^{i\beta_d^{(b)}h_t}\\
T_{3,7} &= -\beta_s^{(b)}e^{-i\beta_s^{(b)}h_t}\\
T_{3,8} &= \beta_s^{(b)}e^{i\beta_s^{(b)}h_t}
\end{aligned} \tag{A3}$$

$$\begin{aligned}
T_{4,1} &= \beta_d^{(t)}e^{-i\beta_d^{(t)}h_t}\\
T_{4,2} &= -\beta_d^{(t)}e^{i\beta_d^{(t)}h_t}\\
T_{4,3} &= -\alpha e^{-i\beta_s^{(t)}h_t}\\
T_{4,4} &= -\alpha e^{i\beta_s^{(t)}h_t}\\
T_{4,5} &= -\beta_d^{(b)}e^{-i\beta_d^{(b)}h_t}\\
T_{4,6} &= \beta_d^{(b)}e^{i\beta_d^{(b)}h_t}\\
T_{4,7} &= \alpha e^{-i\beta_s^{(b)}h_t}\\
T_{4,8} &= \alpha e^{i\beta_s^{(b)}h_t}
\end{aligned} \tag{A4}$$

$$\begin{aligned}
T_{5,1} &= \rho_2\omega^2\beta_d^{(t)}\\
T_{5,2} &= -\rho_2\omega^2\beta_d^{(t)}\\
T_{5,3} &= -\rho_2\omega^2\alpha\\
T_{5,4} &= -\rho_2\omega^2\alpha\\
T_{5,10} &= \beta_2
\end{aligned} \tag{A5}$$

$$\begin{aligned}
T_{6,5} &= \rho_1\omega^2\beta_d^{(b)}e^{-i\beta_d^{(b)}h}\\
T_{6,6} &= -\rho_1\omega^2\beta_d^{(b)}e^{i\beta_d^{(b)}h}\\
T_{6,7} &= -\rho_1\omega^2\alpha e^{-i\beta_s^{(b)}h}\\
T_{6,8} &= -\rho_1\omega^2\alpha e^{i\beta_s^{(b)}h}\\
T_{6,9} &= -\beta_1 e^{-i\beta_1 h}
\end{aligned} \tag{A6}$$

$$\begin{aligned}
T_{7,1} &= -\left(\lambda_t\alpha^2 + (\lambda_t+2\mu_t)\left[\beta_d^{(t)}\right]^2\right)\\
T_{7,2} &= -\left(\lambda_t\alpha^2 + (\lambda_t+2\mu_t)\left[\beta_d^{(t)}\right]^2\right)\\
T_{7,3} &= 2\mu_t\alpha\beta_s^{(t)}\\
T_{7,4} &= -2\mu_t\alpha\beta_s^{(t)}\\
T_{7,10} &= 1
\end{aligned} \tag{A7}$$

$$\begin{aligned}
T_{8,1} &= -2\mu_t\alpha\beta_d^{(t)}\\
T_{8,2} &= 2\mu_t\alpha\beta_d^{(t)}\\
T_{8,3} &= \mu_t\left(\alpha^2 - \left[\beta_s^{(t)}\right]^2\right)\\
T_{8,4} &= \mu_t\left(\alpha^2 - \left[\beta_s^{(t)}\right]^2\right)
\end{aligned} \tag{A8}$$

$$\begin{aligned}
T_{9,5} &= -\left(\lambda_b\alpha^2 + (\lambda_b+2\mu_b)\left[\beta_d^{(b)}\right]^2\right)e^{-i\beta_d^{(b)}h}\\
T_{9,6} &= -\left(\lambda_b\alpha^2 + (\lambda_b+2\mu_b)\left[\beta_d^{(b)}\right]^2\right)e^{i\beta_d^{(b)}h}\\
T_{9,7} &= 2\mu_b\alpha\beta_s^{(b)}e^{-i\beta_s^{(b)}h}\\
T_{9,8} &= -2\mu_b\alpha\beta_s^{(b)}e^{i\beta_s^{(b)}h}\\
T_{9,9} &= e^{-i\beta_1 h}
\end{aligned} \tag{A9}$$

$$\begin{aligned}
T_{10,5} &= -2\mu_b\alpha\beta_d^{(b)}e^{-i\beta_d^{(b)}h}\\
T_{10,6} &= 2\mu_b\alpha\beta_d^{(b)}e^{i\beta_d^{(b)}h}\\
T_{10,7} &= \mu_b\left(\alpha^2 - \left[\beta_s^{(b)}\right]^2\right)e^{-i\beta_s^{(b)}h}\\
T_{10,8} &= \mu_b\left(\alpha^2 - \left[\beta_s^{(b)}\right]^2\right)e^{i\beta_s^{(b)}h}
\end{aligned} \tag{A10}$$

The nonzero entries of [U(α)] matrix are:

$$
\begin{aligned}
U_{9,5} &= -\frac{i\widehat{K}_y\beta_d^{(b)}}{L}e^{-i\beta_d^{(b)}h}\\
U_{9,6} &= \frac{i\widehat{K}_y\beta_d^{(b)}}{L}e^{i\beta_d^{(b)}h}\\
U_{9,7} &= \frac{i\widehat{K}_y\alpha}{L}e^{-i\beta_s^{(b)}h}\\
U_{9,8} &= \frac{i\widehat{K}_y\alpha}{L}e^{i\beta_s^{(b)}h}
\end{aligned}
\tag{A11}
$$

$$
\begin{aligned}
U_{10,5} &= -\frac{\widehat{K}_x\alpha_n\beta_d^{(b)}}{L}e^{-i\beta_d^{(b)}h}\\
U_{10,6} &= \frac{\widehat{K}_x\alpha_n\beta_d^{(b)}}{L}e^{i\beta_d^{(b)}h}\\
U_{10,7} &= \frac{\widehat{K}_x\alpha_n\alpha}{L}e^{-i\beta_s^{(b)}h}\\
U_{10,8} &= \frac{\widehat{K}_x\alpha_n\alpha}{L}e^{i\beta_s^{(b)}h}
\end{aligned}
\tag{A12}
$$

The entries of the generalized force vector are:

$$
\mathrm{F} = \begin{bmatrix} 0 & 0 & 0 & 0 & 0 & 0 & 0 & 0 & -q_0e^{i\alpha x_0} & 0 \end{bmatrix}^{\mathrm{T}} \tag{A13}
$$

References

Berry, A., Foin, O., Szabo, J.P., 2001. Three-dimensional elasticity model for a decoupling coating on a rectangular plate immersed in a heavy fluid. J. Acoust. Soc. Am. 109 (6), 2704–2714.

Chen, Y.Y., Huang, G.L., 2015. Active elastic metamaterials for subwavelength wave propagation control. Acta Mech. Sin. 31 (3), 349–363.

Chonan, S., Kugo, Y., 1991. Acoustic design of a three-layered plate with high sound interception. J. Acoust. Soc. Am. 89 (2), 792–798.

David, J. Steigmann, Francesco, dell'Isola, 2015. Mechanical response of fabric sheets to three-dimensional bending, twisting, and stretching. Acta Mech. Sin. 31 (3), 373–382.

Ehsan Omidi, S.N.M., 2016. Nonlinear integral resonant controller for vibration reduction in nonlinear systems. Acta Mech. Sin. 32 (5), 925–934.

Foin, O., Berry, A., Szabo, J., 2000. Acoustic radiation from an elastic baffled rectangular plate covered by a decoupling coating and immersed in a heavy acoustic fluid. J. Acoust. Soc. Am. 107 (5), 2501–2510.

Gholami, R., Darvizeh, A., Ansari, R., Sadeghi, F., 2016. Vibration and buckling of first-order shear deformable circular cylindrical micro-/nano-shells based on mindlin's strain gradient elasticity theory. Eur. J. Mech. A Solid 58, 76–88.

Hao, A., Zhao, H., Chen, J.Y., 2013. Kenaf/polypropylene nonwoven composites: the influence of manufacturing conditions on mechanical, thermal, and acoustical performance. Compos. Part B Eng 54 (0), 44–51.

Hasheminejad, S.M., Miri, A.K., 2007. Dynamic interaction of an eccentric multipole cylindrical radiator suspended in a fluid-filled borehole within a poroelastic formation. Acta Mech. Sin. 23 (4), 399–408.

Hladky-Hennion, A.C., Decarpigny, J.N., 1991. Analysis of the scattering of a plane acoustic wave by a doubly periodic structure using the finite element method: application to alberich anechoic coatings. J. Acoust. Soc. Am. 90 (6), 3356–3367.

Jackins, P.D., Gaunaurd, G.C., 1986. Resonance acoustic scattering from stacks of bonded elastic plates. J. Acoust. Soc. Am. 80 (6), 1762–1776.

Keltie, R.F., 1993. Structural acoustic response of finite rib-reinforced plates. J. Acoust. Soc. Am. 94 (2), 880–887.

Keltie, R.F., 1998. Signal response of elastically coated plates. J. Acoust. Soc. Am. 103 (4), 1855–1863.

Ko, S.H., 1997. Reduction of structure-borne noise using an air-voided elastomer. J. Acoust. Soc. Am. 101 (6), 3306–3312.

Legault, J., Atalla, N., 2010. Sound transmission through a double panel structure periodically coupled with vibration insulators. J. Sound. Vib. 329 (15), 3082–3100.

Li, F.-M., Lyu, X.-X., 2014. Active vibration control of lattice sandwich beams using the piezoelectric actuator/sensor pairs. Compos. Part B Eng 67, 571–578.

Li, D., Liu, Y., Zhang, X., 2013. A layerwise/solid-element method of the linear static and free vibration analysis for the composite sandwich plates. Compos. Part B Eng 52 (0), 187–198.

Liang, J.-Z., Jiang, X.-H., 2012. Soundproofing effect of polypropylene/inorganic particle composites. Compos. Part B Eng 43 (4), 1995–1998.

Lin, G.-F., Garrelick, J.M., 1977. Sound transmission through periodically framed parallel plates. J. Acoust. Soc. Am. 61 (4), 1014–1018.

Mace, B.R., 1980. Sound radiation from a plate reinforced by two sets of parallel stiffeners. J. Sound. Vib. 71 (3), 435–441.

Mace, B.R., 1981. Sound radiation from fluid loaded orthogonally stiffened plates. J. Sound. Vib. 79 (3), 439–452.

Maidanik, G., Tucker, A.J., 1974. Acoustic properties of coated panels immersed in fluid media. J. Sound. Vib. 34 (4), 519–550.

Mejdi, A., Atalla, N., 2010. Dynamic and acoustic response of bidirectionally stiffened plates with eccentric stiffeners subject to airborne and structure-borne excitations. J. Sound. Vib. 329 (21), 4422–4439.

Mejdi, A., Atalla, N., 2012. Vibroacoustic analysis of laminated composite panels stiffened by complex laminated composite stiffeners. Int. J. Mech. Sci. 58 (1), 13–26.

Mindlin, R.D., 1951. Influence of rotatory inertia and shear on flexural motions of isotropic elastic plates. J. Appl. Mech. Trans. ASME 18 (1), 31–38.

Narayanan, S., Shanbhag, R.L., 1981. Sound transmission through elastically supported sandwich panels into a rectangular enclosure. J. Sound. Vib. 77 (2), 251–270.

Pandey, S., Pradyumna, S., 2015. Free vibration of functionally graded sandwich plates in thermal environment using a layerwise theory. Eur. J. Mech. A Solid 51, 55–66.

Park, J., Mongeau, L., 2008. Vibration and sound radiation of viscoelastically supported mindlin plates. J. Sound. Vib. 318 (4–5), 1230–1249.

Qu, Y., Meng, G., 2014. Three-dimensional elasticity solution for vibration analysis of functionally graded hollow and solid bodies of revolution. Part I: Theory. Eur. J. Mech. A Solid 44, 222–233.

Reza Ansari, J.T., 2016. Nonlocal vibration analysis of circular double-layered graphene sheets resting on an elastic foundation subjected to thermal loading. Acta Mech. Sin. 32 (5), 841–853.

Sadeghpour, E., Sadighi, M., Ohadi, A., 2016. Free vibration analysis of a debonded curved sandwich beam. Eur. J. Mech. A Solid 57, 71–84.

Sahoo, S.S., Panda, S.K., Mahapatra, T.R., 2016. Static, free vibration and transient response of laminated composite curved shallow panel – an experimental approach. Eur. J. Mech. A Solid 59, 95–113.

Tao, M., Tang, W.L., Hua, H.X., 2010. Noise reduction analysis of an underwater decoupling layer. ASME J. Vib. Acoust. 132 (6), 061006.

Xin, F.X., Lu, T.J., 2010a. Analytical modeling of fluid loaded orthogonally rib-stiffened sandwich structures: sound transmission. J. Mech. Phys. Solids 58 (9), 1374–1396.

Xin, F.X., Lu, T.J., 2010b. Sound radiation of orthogonally rib-stiffened sandwich structures with cavity absorption. Compos. Sci. Technol. 70 (15), 2198–2206.

Xin, F.X., Lu, T.J., 2016. Acoustomechanical constitutive theory for soft materials. Acta Mech. Sin. 32 (5), 828–840.